LETTER

In Situ Observation of Sodium Dendrite Growth and Concurrent Mechanical Property Measurements Using an Environmental Transmission Electron Microscopy–Atomic Force Microscopy (ETEM-AFM) Platform

Qiunan Liu, Liqiang Zhang,* Haiming Sun, Lin Geng, Yanshuai Li, Yushu Tang, Peng Jia, Zaifa Wang, Qiushi Dai, Tongde Shen, Yongfu Tang,* Ting Zhu, and Jianyu Huang*

Read Online

ACCESS | Metrics & More | Article Recommendations | Supporting Information

ABSTRACT: Akin to Li, Na deposits in a dendritic form to cause a short circuit in Na metal batteries. However, the growth mechanisms and related mechanical properties of Na dendrites remain largely unknown. Here we report real-time characterizations of Na dendrite growth with concurrent mechanical property measurements using an environmental transmission electron microscopy–atomic force microscopy (ETEM-AFM) platform. *In situ* electrochemical plating produces Na deposits stabilized with a thin Na_2CO_3 surface layer (referred to as Na dendrites). These Na dendrites have characteristic dimensions of a few hundred nanometers and exhibit different morphologies, including nanorods, polyhedral nanocrystals, and nanospheres. *In situ* mechanical measurements show that the compressive and tensile strengths of Na dendrites with a Na_2CO_3 surface layer vary from 36 to >203 MPa, which are much larger than those of bulk Na. *In situ* growth of Na dendrites under the combined overpotential and mechanical confinement can generate high stress in these Na deposits. These results provide new baseline data on the electrochemical and mechanical behavior of Na dendrites, which have implications for the development of Na metal batteries toward practical energy-storage applications.
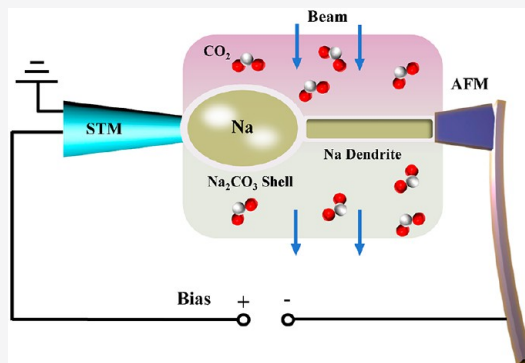
Sodium (Na) metal batteries (SMBs), an alternative to lithium (Li) metal batteries (LMBs), have recently attracted substantial attention due to their high specific capacity, abundance of Na supply, and low cost.[1−5] Akin to Li, Na deposits in a dendritic form to cause a short circuit in SMBs, impeding the development of high-performance SMBs.[6−9] Extensive research has been conducted on the mechanisms of Li dendrite growth and deposition in the literature.[10−14] However, studies of Na dendrite growth and Na plating are scarce. There are only a few optical studies on Na deposition,[15−18] which show the formation of Na deposits in a dendritic form with a root growth mechanism in liquid electrolytes. Several recent studies reveal how Na deposits or grows in an all-solid SMB.[19,20] The mechanical properties of bulk Na were investigated systematically by Fincher et al.[21] at room temperature through a combination of bulk compression, microhardness, and nanoindentation tests. They reported a

Young's modulus of ∼3.9 GPa, a flow stress at 8% strain varying between 0.1 and 0.25 MPa at strain rates between 0.01 and 1% s^{-1}, and a microhardness ranging from 1.1 to 1.6 MPa. Their studies indicate that Na metal is extremely soft, readily creeps, and exhibits pronounced size effects. These results provide an important understanding of the mechanical behavior of bulk and microscale Na. However, hitherto, there is no direct characterization of the growth and mechanical behavior of nanoscale Na deposits stabilized with solid electrolyte interphases (SEIs), mainly due to technical
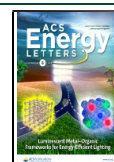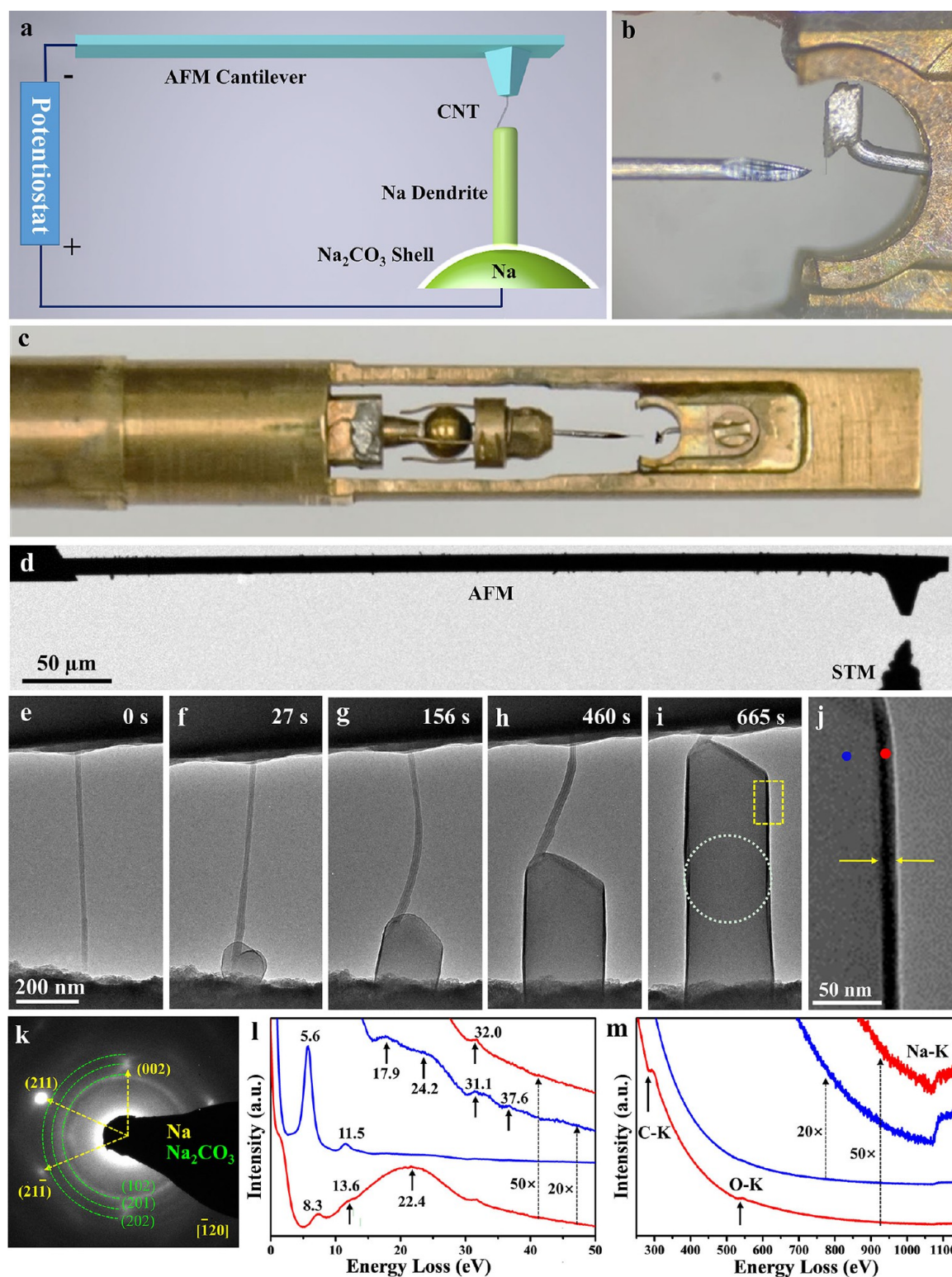
Figure 1. (a) Schematic of the ETEM-AFM setup for *in situ* studies of Na dendrite. An arc-discharged CNT was attached to a conducting AFM tip by electron beam deposition of carbonaceous material, which was used as a cathode; a sharp W needle attached to scratched Na was used as an anode; and naturally formed Na_2CO_3 on the Na surface was used as an electrolyte. (b,c) High- and low-magnification optical images of the ETEM-AFM device. (d) TEM image showing an AFM cantilever tip approaching the counter electrode of Na metal attached to a scanning tunneling microscopy (STM) probe. (e−i) Time-lapse TEM images showing the growth of a Na dendrite via electrochemical plating. A bias of −3.0 V was applied to initiate the Na dendrite growth. After 665 s, a Na dendrite with a length of 825 nm and a diameter of 260 nm was generated, and its aspect ratio is 3.2. (j) Local magnified image of panel i marked by the yellow rectangle. (k) EDP of the Na dendrite, showing diffraction spots superimposed on diffraction rings, which are indexed as the $[\bar{1}20]$ zone axis of Na. A thin layer of Na_2CO_3 is formed on the surface of the Na dendrite. (l) Low-loss and (m) core-loss EELS of the Na dendrite (blue plot) and Na_2CO_3 (red plot), respectively.
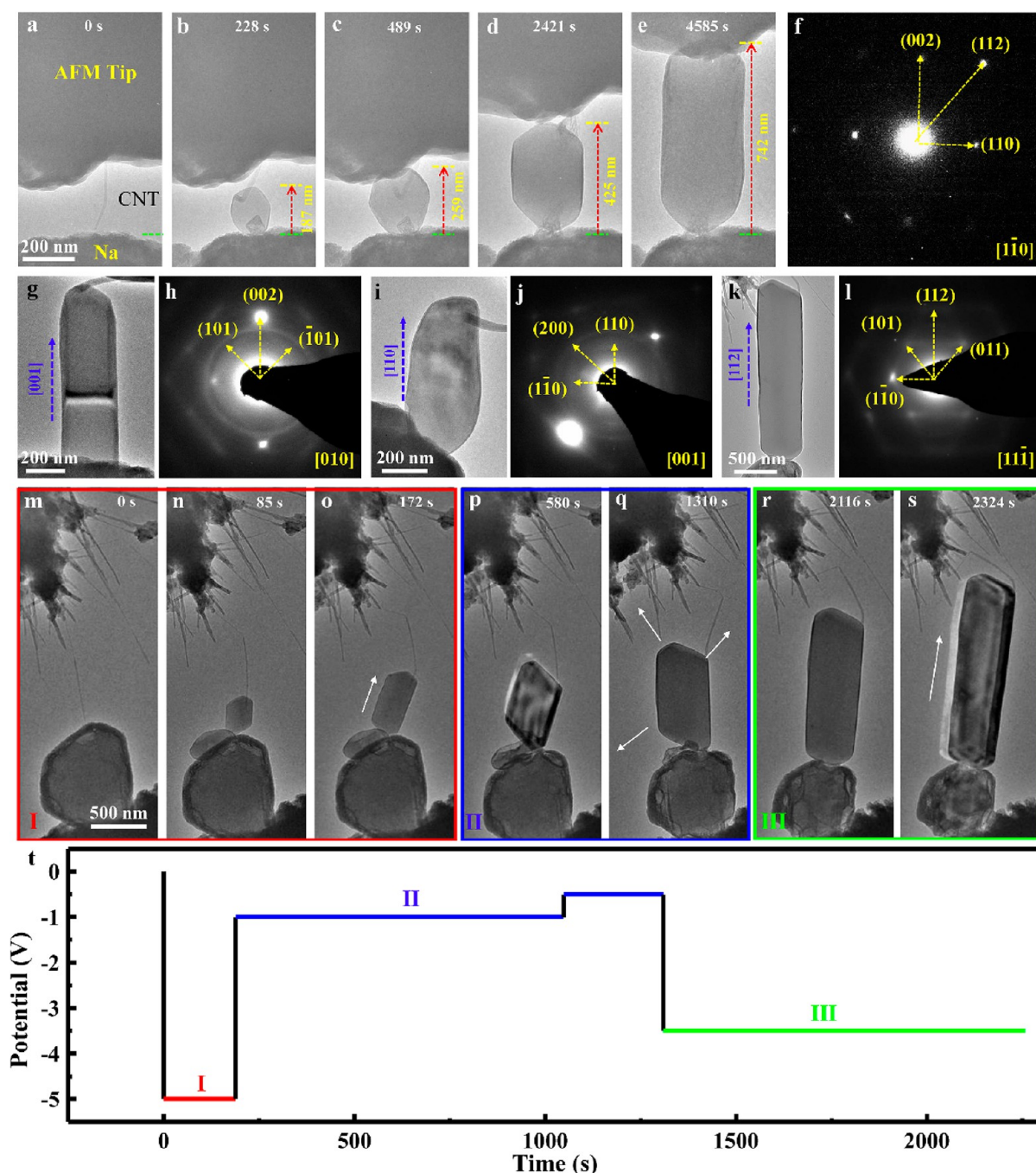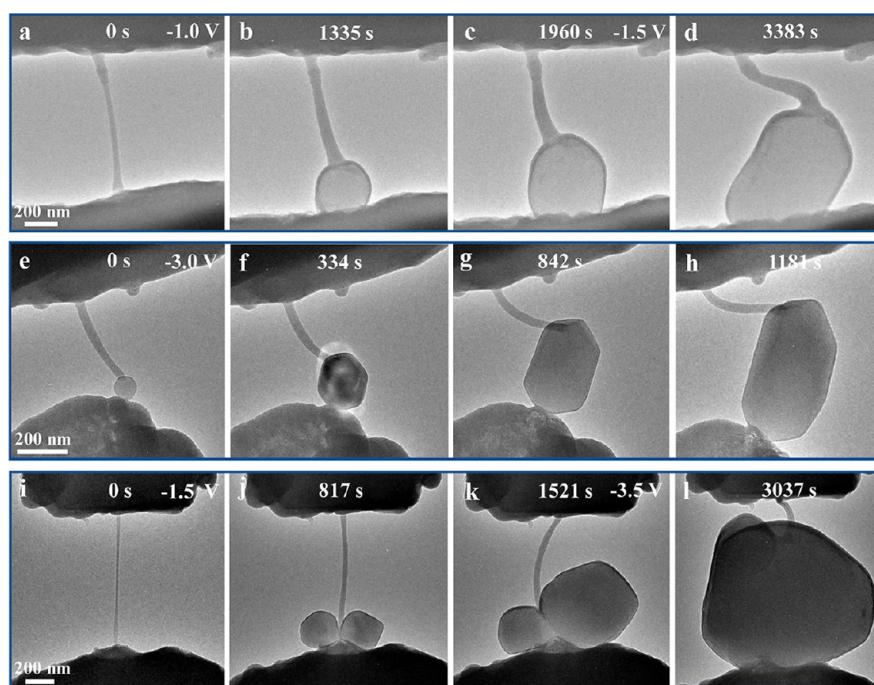
Figure 2. Time-lapse TEM images showing the growth of Na dendrites via electrochemical plating. (a,b) Upon applying a negative potential to the CNT against the Na anode, a nanosphere emerged at the CNT, Na_2CO_3, and CO_2 triple point. (c,d) The nanosphere grew and was faceted with the lapse of time. (e) The nanosphere evolved into a nanorod with a diameter of 309 nm, a length of 742 nm, and an aspect ratio of 2.40. (f) An EDP of the nanorod, which can be indexed as $[1\bar{1}0]$ zone axis of metallic Na. The EDP indicates that the growth direction of the nanorod shown in panel e is [001]. (g–l) The Na dendrites grew along the (g,h) [001], (i,j) [110], and (k,l) [112] directions, respectively. (m–s) Time-lapse TEM images of Na dendrite growth under different overpotentials. When the CNT and metal Na were connected, an external bias (−5.0 V) was supplied to initiate Na dendrite growth, and the dendrite grew along one direction with a high speed (m–o). Afterward, the potential was reduced to −1.0 and −0.5 V, under which the dendrite grew in all directions with a slow rate (p,q). When the potential was increased to −3.5 V again, the Na dendrite resumed its initial growth direction (r,s). (t) The potential−time plot corresponds to the dendrite growth shown in panels m–s.

difficulties in fabricating samples that are suitable for nanomechanical tests. Such characterization is essential to understanding the electro-chemo-mechanical response of Na dendrites and associated SEIs during cycling, so as to mitigate Na dendrite growth toward the development of high-performance SMBs. Here we created a novel all-solid-state electrochemical device that consists of a Na metal anode, a Na_2CO_3 electrolyte, and a cathode with a carbon nanotube (CNT) attached to the tip of an atomic force microscope (AFM), which operated in a CO_2 atmosphere within an aberration-corrected environmental transmission electron microscope (ETEM, Figure 1a−d). This electro-chemo-

Figure 3. Three sets of time-lapse TEM images showing the growth of Na dendrites. (a−d) Detailed growth process of a dendrite. Initially, a spherical Na nanoparticle emerged under a low voltage (−1.0 V) (b), which slowly evolved into a faceted nanorod under a continuous low voltage (−1.5 V) (c,d). (e−h) Detailed growth process of a faceted nanorod. Initially, a Na nanosphere emerged (e), which quickly evolved into a polyhedral crystal (f), and elongated polyhedral crystals (g,h) under a constant bias of −3 V. (i−l) Detailed growth process of a spherical dendrite. (i) Starting electrochemical plating device. Initially, two faceted nanoparticles appeared under −1.5 V (j), which gradually increased their size as the voltage was ramped up (k). The Na crystal on the right continued its growth, while the one on the left appeared to be merged with the right Na crystal (l).

mechanical device (referred to as ETEM-AFM)[22,23] enables not only *in situ* observations of the electrochemical plating of Na but also real-time measurements of the mechanical properties of as-deposited nanoscale Na, thereby facilitating simultaneous electro-chemo-mechanical characterizations of Na deposits stabilized with a Na_2CO_3 surface layer.

Using the novel ETEM-AFM platform, the electrochemical deposition of Na, the formation of the SEI, and their mechanical properties were characterized in real time. Results show that Na deposits were stabilized by a Na_2CO_3 surface layer and exhibit various morphologies such as nanorods (with low aspect ratio), nanospheres, nanocubes, and polyhedral nanocrystals. These nanostructures have the characteristic sizes of a few hundred nanometers and are covered by an SEI layer of Na_2CO_3 with a thickness of <20 nm. Hereafter, these Na deposits are referred to as Na dendrites. The compressive and tensile strengths of Na dendrites vary from 36 to 203 MPa, which is much higher than that of bulk Na,[21] and the Young's modulus varies from 1.3 to 3.5 GPa. The compressive strength of Na_2CO_3 varies from 261 to 692 MPa. These results provide new baseline data on and insight into the electrochemical and mechanical properties of Na dendrites stabilized with an SEI surface layer of Na_2CO_3.

Our experiments were conducted in an aberration-corrected ETEM, which permits a certain gas such as CO_2 to flow into the sample chamber up to 20 mbar. The ETEM-AFM platform was built in a special TEM sample holder integrated with a piezo-manipulator (Pico-Femto F20). An arc-discharged carbon nanotube (CNT) was attached to a conductive AFM tip. This CNT-AFM assembly was used as the cathode of the electrochemical ETEM-AFM device (Figure 1a−d). A sharp

tungsten (W) tip attached to a piece of Na metal was used as the anode. Na_2CO_3 was formed on the surface of Na metal and served as the solid electrolyte (Figure S1).[24]

Upon applying a negative potential to the CNT against the Na metal electrode, the nanotube swelled due to a combined effect of the intercalation of Na^+ ions into the CNT and the formation of an SEI layer on the surface of the CNT (Figure 1e,f, Movie S1). After the CNT swelled from 20 to ∼28 nm, a ball with size of 136 nm emerged at the triple point of the CNT, Na_2CO_3, and CO_2 (Figure 1f); the ball then grew to form facets and finally became a dendrite with an aspect ratio of ∼3.2 (Figure 1g−i). The electron diffraction pattern (EDP) of the dendrite (Figure 1k) exhibits diffraction rings superimposed with diffraction spots, which are indexed as Na_2CO_3 and Na, respectively. The diffraction spot pattern is indexed as the $[\bar{1}20]$ zone axis of Na, indicating that the dendrite is a single crystal with the growth direction of [001]. Electron energy-loss spectroscopy (EELS, Figure 1l,m) from the dendrite indicate that its inner core is metallic Na while its surface is covered by a thin layer of Na_2CO_3 with a thickness of 14 nm (Figure 1j). The formation of Na_2CO_3 resulted from the chemical reaction of $Na + CO_2 \rightarrow Na_2CO_3 + C$ or CO. The thickness of the Na_2CO_3 layer increased slowly with time and reached the maximum thickness of <20 nm after prolonged dendrite growth (Figure S2). It should be noted that the SEI layer of Na_2CO_3 on Na was previously observed on the electrochemically deposited Na in propylene-carbonate (PC)-based electrolyte.[25]

Most Na dendrites in our experiments grew along the [001] direction (Figure 2a−h, Movie S2), and a few dendrites grow along [110] (Figure 2i,j) and [112] (Figure 2k,l). These results
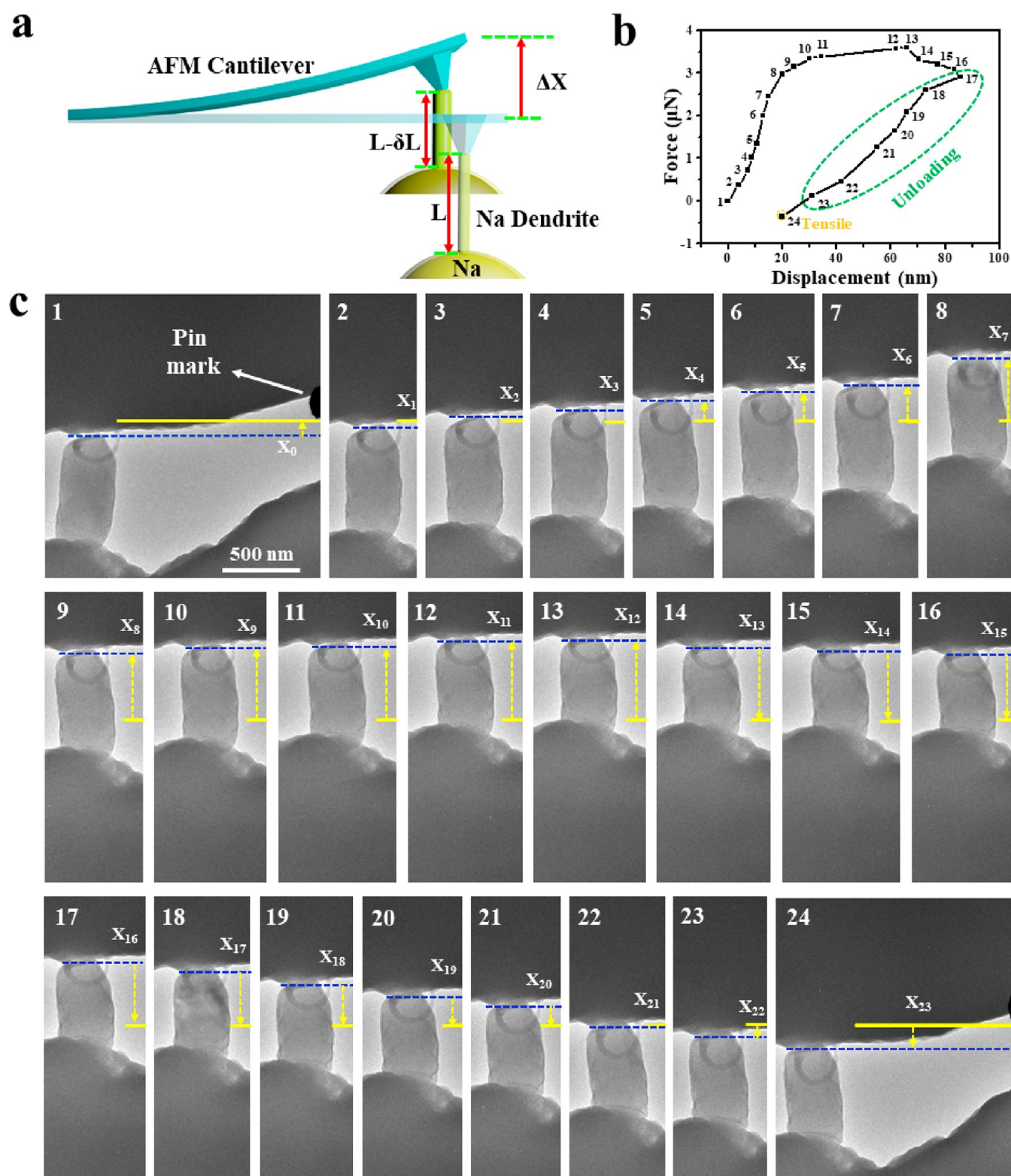
Figure 4. (a) Schematic of the ETEM-AFM setup used for measurement *in situ* compression of the as-grown Na dendrite. When the Na dendrite is pushed upward, the AFM cantilever is bent upward with a tip displacement of ΔX, while the Na dendrite is compressed from its initial length of L to $L - \delta L$ because of the force exerted on it by the AFM tip. The force is calculated as $k \cdot \Delta X$, where k is the force constant of the AFM cantilever. The strain of the dendrite is $\delta L/L$. The spring constant of the Si AFM cantilever beam is $k = 6$ N m^{-1}. Each data point in the force−displacement curve in panel b is provided as a "picture-to-point" montage in panel c. The displacement of the AFM cantilever was measured using a beam blocking bar (the dark object on the upper-right corner of frames 1 and 24 in panel c) as a reference. The beam blocking bar remained unchanged during the entire mechanical testing. To save space, the beam blocking bar is not shown in every image, but its position is marked by a solid horizontal yellow line in each frame. No dislocation activity was observed during the compression experiment; instead, the dendrite deformed by diffusion induced mass flow, which led to a slight diameter increase accompanied by a length reduction. The corresponding mechanical data are shown in Table S1. The thickness of the Na$_2$CO$_3$ surface layer is 14 nm.
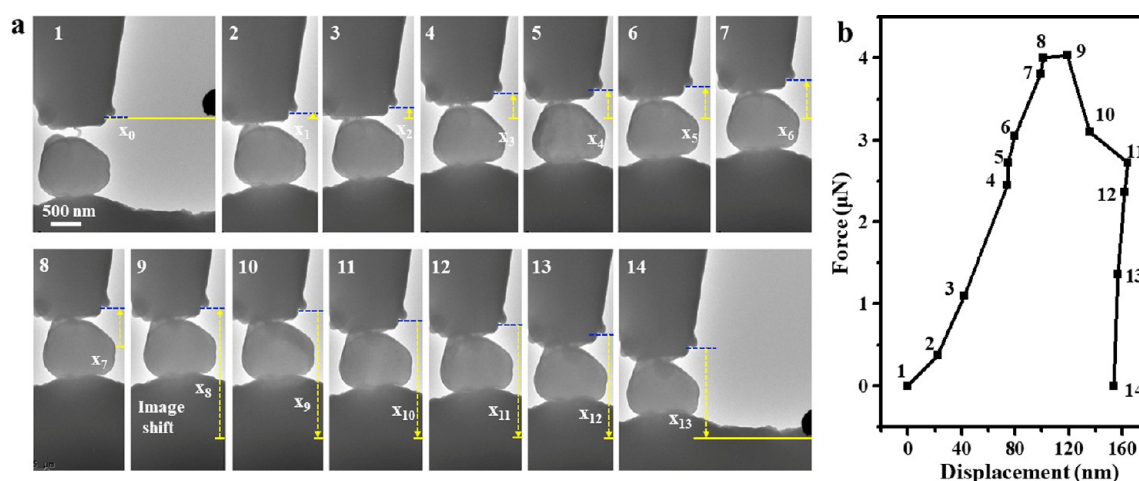
Figure 5. (a) Sequential TEM images showing the compression and unloading process for a Na nanoparticle. The corresponding force−displacement curve is shown in panel b. Each data point in the force−displacement curve (b) was measured according to the images shown in panel a, referred to as "picture-to-point" montage. The displacement of the AFM cantilever was measured using a beam blocking bar (the dark object on the upper-right corner of frames 1 and 14 in panel a) as a reference. Note the lack of dislocation activity during the compression experiment. The corresponding mechanical data are shown in Table S3. The thickness of the Na_2CO_3 surface layer is 18 nm.
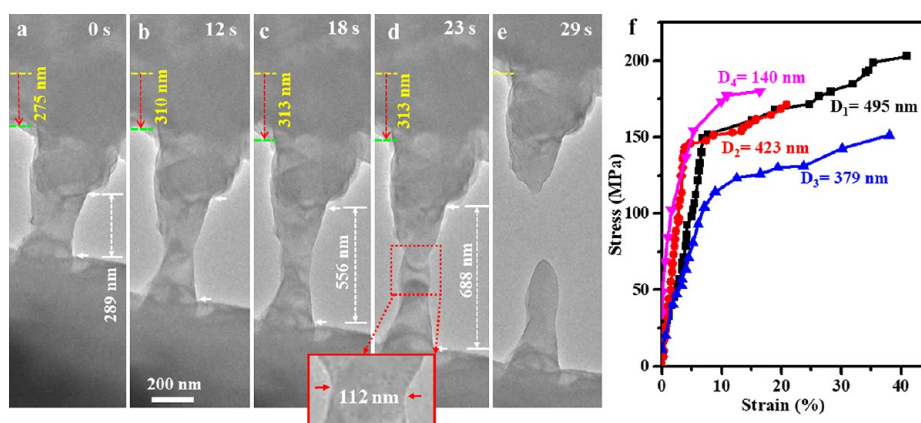

Figure 6. *In situ* tensile experiment of a Na dendrite. The spring constant of the Si AFM cantilever beam is $k = 3$ N m^{-1}. (a−e) Because of the high viscosity of sodium metal, the Na dendrite and AFM can be well connected together after growth; therefore, the tensile test can be successfully carried out. When the displacement of the AFM tip reached ~313 nm, the Na dendrite broke in the middle. (f) Typical tensile stress−strain curves for several Na dendrites with different diameters. From the linear elastic regions, the Young's modulus was deduced to be from 1.3 to 3.5 GPa. The dark and red curves correspond to Figure S9a−d and Figure S9e−h, respectively. The thickness of the surface Na_2CO_3 layer is 2 nm.

demonstrate that Na dendrites can be easily produced via the present electrochemical plating method. The applied voltage is a critical parameter to control the morphologies of deposited Na dendrites. As shown in Figure 2m−t, a small faceted Na nanocrystal grew on top of a bigger faceted Na nanocrystal (Figure 2m−o, Movie S3). When a high external bias (−5.0 V) was applied between the CNT and Na metal, the dendrite predominantly grew along one direction (indicated by the white arrow in Figure 2o) with a high speed, exhibiting a slender dendritic morphology. When a low potential of −1.0 or −0.5 V was applied, the dendrite grew in all directions (white arrows in Figure 2q) at a slow rate. By increasing the potential to −3.5 V again, the Na dendrite turned to the predominant growth along one direction (white arrow in Figure 2s), indicating that the growth mode can be controlled by voltage. During the dendrite growth process, the electrical current (*I*) in the Na dendrite was recorded by an ampere meter (Figure S3).

In addition to dendrites in a nanorod shape, Na was deposited as polyhedral nanocrystals, nanocubes, and nanoparticles under different voltages (Figure 3, Figures S4 and S5, and Movies S4−S8). It is noted that when Na dendrites were deposited in the high vacuum of ETEM with no external gas supply, they were unstable and easily collapsed under electron beam irradiation (Figure S6). In contrast, Na dendrites grown in a CO_2 environment with a thin SEI layer of Na_2CO_3 formed on their surface were stable under electron beam illumination, thus enabling further in-depth studies of growth, mechanical properties, and electro-chemo-mechanical responses of Na dendrites. A similar phenomenon of the growth of Li dendrites stabilized by surface SEI was previously observed,[23] underscoring the importance of ETEM, as opposed to conventional TEM, in the studies of alkali metals such as Li and Na.

As-deposited Na dendrites were subjected to either *in situ* compressive or tensile loading to measure their mechanical properties (Figures 4−6, Figures S7−S9, Movies S9−S17). Figure 4 (Movie S9) shows the *in situ* compression of a Na

Table 1. Critical Stress σ for a Series of Na Dendrites Stabilized with a Na$_2$CO$_3$ Surface Layer and Na$_2$CO$_3$ with Different Shapes and Diameters[a]

| | Na | | | | | | | | | Na$_2$CO$_3$ | | | |
| | nanorods (compression) | | | nanoparticles (compression) | | | nanorods (tensile) | | | nanospheres (compression) | | nanopillar (compression) | |
	diameter (nm)	growth direction	σ (MPa)	diameter (nm)	growth direction	σ (MPa)	diameter (nm)	growth direction	σ (MPa)	diameter (nm)	σ (MPa)	diameter (nm)	σ (MPa)
1	235	[110]	113	1110	[112]	97	435	*	110	524	303	140	261
2	253	[001]	131	404	[110]	139	495	*	203	724	367	45	317
3	247	*	106	655	[112]	151	423	*	187	657	660	53	455
4	361	[001]	111	659	[112]	174	379	*	151	242	692	40	336
5	322	*	126	878	[110]	92	196	*	95	772	348	150	511

[a]Critical stress refers to the compressive stress and maximum tensile stress measured from compression and tension tests, respectively. The strain rate is ~1.7×10^{-3} s^{-1}. (* means the growth direction is unknown.)
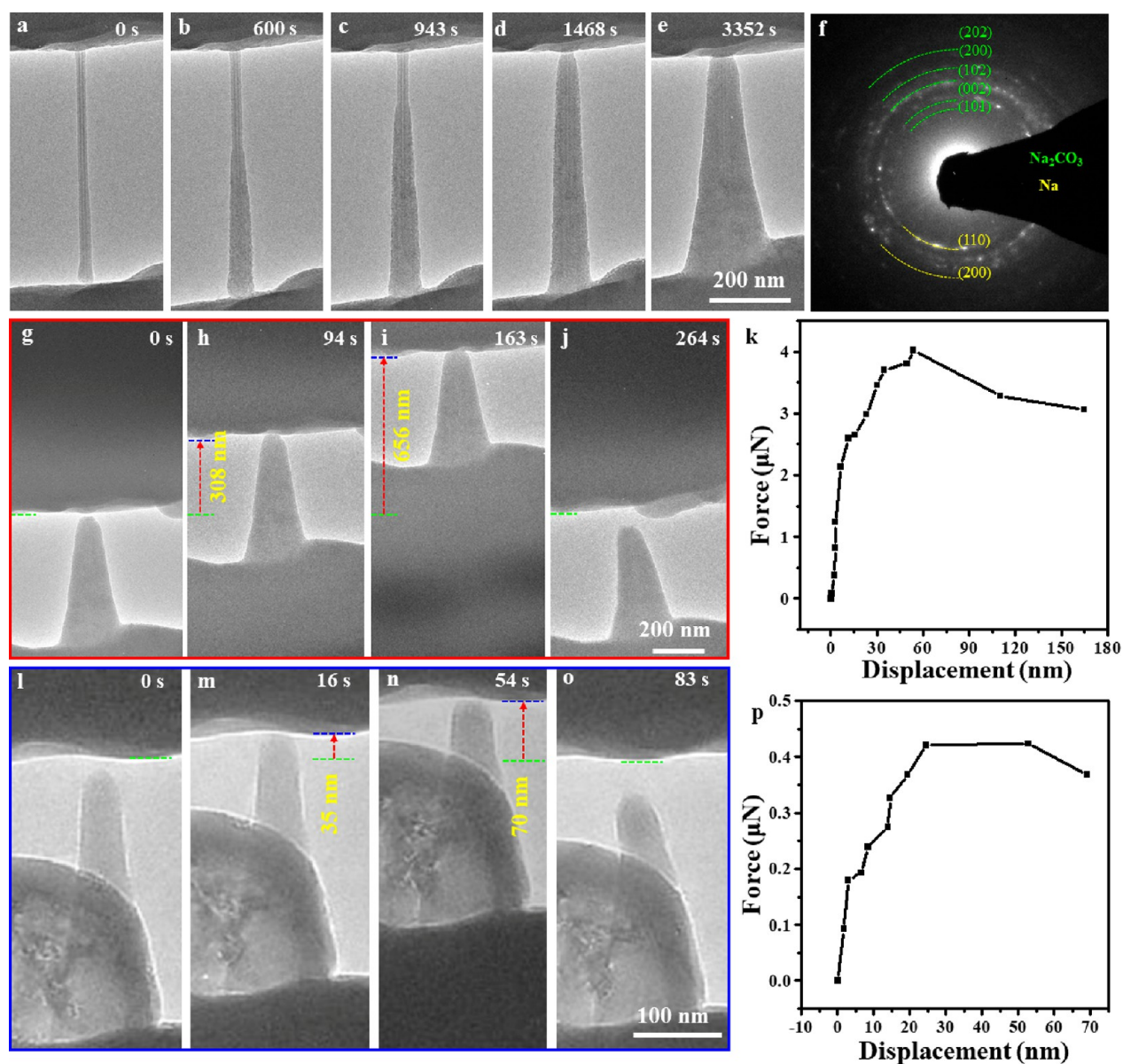
Figure 7. *In situ* TEM images showing the growth of a Na$_2$CO$_3$ pillar. The spring constant of the Si AFM cantilever beam is $k = 6$ N m^{-1}. (a–e) Upon applying a negative potential of −4.0 V to the CNT against the Na anode, Na atoms or ions quickly climbed up along the CNT. Because of the CO$_2$ environment in the ETEM, it entirely turned into a Na$_2$CO$_3$ pillar with only a little metal Na residue (f). Panels g–j and l–o are two sets of *in situ* compression experiments of Na$_2$CO$_3$ pillars, and the compression strengths were calculated to be 261 and 336 MPa for the former and latter, respectively. (k,p) Force–displacement curves corresponding to the *in situ* compression tests (g–j) and (l–o), respectively.
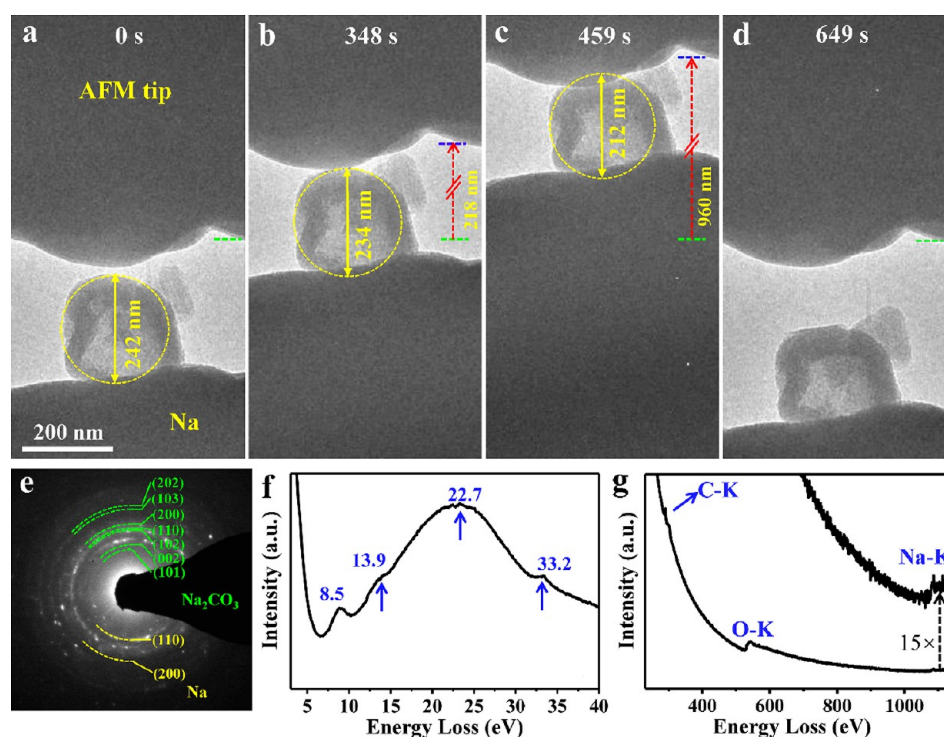
Figure 8. (a−d) *In situ* compression test of a Na_2CO_3 hollow nanosphere. The spring constant of the Si AFM cantilever beam is $k = 6$ N m^{-1}. (e) The EDP of the Na_2CO_3 hollow nanosphere exhibits a little metallic Na residue. (f) Low-loss and (g) core-loss EELS of the Na_2CO_3 hollow nanosphere.

dendrite. As the dendrite was pushed up by the Na metal electrode, the AFM cantilever moved upward accordingly (Figure 4a). Because the force constant k of the AFM cantilever is already known, and from the displacement of the AFM cantilever, the force (F) exerted on the AFM cantilever can be calculated from Hooke's law $F = k \times \Delta X$,[26] where k is the force constant of the AFM cantilever and ΔX is the displacement of the AFM tip. The length and diameter changes of the dendrite during compression are directly obtained from *in situ* TEM images. The corresponding force−displacement curve is shown in Figure 4b. A similar method has been recently applied to characterize the mechanical properties of individual Li dendrites[22,23] and other nanowires.[27,28] Prior to the mechanical experiment, we tilted the dendrite to different angles for an accurate measurement of its cross-sectional geometry (Figures S10−S12). After the compression test, the diameter and length of the dendrite changed from the initial 355 and 776 nm to 385 and 678 nm, respectively (Figure 4c). The maximum compressive force is 3.6 μN (Figure 4b). When we use the contact area as an approximate cross-sectional area, we obtain a contact stress of 120 MPa; when we use the maximum diameter in the middle of the nanorod to estimate the cross-sectional area, the compressive stress is 36 MPa. We conducted compression experiments on multiple Na nanorods and measured the compressive strength σ in the range of 36 to 131 MPa (Table 1). It should be noted that the nanorod appeared to be slightly bent in both the late stage of loading and the unloading process, as revealed by the *in situ* TEM images (Figure 4c, from the image labeled as "13" on). The corresponding data points labeled as "13" and on in Figure 4b need to be treated with precaution as a bending component affects the nominal uniaxial force−displacement plot.

Figure 5 (Movie S10) shows an *in situ* compression experiment conducted on another Na dendrite. This polyhedron-shaped dendrite was faceted and became slightly flattened during compression. Considering the polyhedral dendrite as a sphere, we calculated the stress in this dendrite in terms of the compression of a sphere between two rigid flat plates based on the Hertzian theory.[29,30] The critical quantity that affects this calculation is the effective contact area. Following the model provided by Mook et al.,[31] we calculated the contact area using the following formula for small to intermediate deformation

$$a_1 = \left(\delta_t r - \frac{\delta_t^2}{4} \right)^{1/2}$$

(1)

where δ_t is the height change of the nanosphere and r is the radius of the nanosphere. This equation is appropriate at small to intermediate deformation, where plastic flow occurs with $\delta_t/2r < 10\%$. For large plastic deformation, say $\delta_t/2r > 10\%$, the following formula was used to estimate the contact area

$$a_2 = \left(\frac{4r^3}{3(2r - \delta_t)} \right)^{1/2}$$

(2)

This formula was derived based on a model of a sphere as a barrel. Using eq 1, the compressive stress for the nanosphere shown in Figure 5 was calculated to be 97 MPa. We conducted compression experiments on multiple nanoparticles and obtained the compressive strength in the range of 92−174 MPa (Table 1).

Tensile experiments were also conducted on as-deposited dendrites (Figure 6 and Figure S9, Movie S11, and Movies S15−S17). Some dendrites adhered to the AFM tip after growth, thus permitting *in situ* tensile tests. During these tensile experiments, we observed obvious necking (Figure 6), which is a typical phenomenon during the tensile loading of

ductile materials. From the displacement of the AFM cantilever (giving the force applied to the dendrite), the maximum tensile stress was calculated to be 95 MPa. We conducted tensile experiments for multiple Na dendrites and obtained the maximum tensile stress in the range of 95−203 MPa (Table 1). Typical tensile stress−strain curves are displayed in Figure 6f, and they exhibit a linear elastic regime followed by plastic yielding and strain hardening. From the linear elastic regime, Young's modulus was determined from 1.3 to 3.5 GPa. Similar to the compressive experiments, strain hardening was observed during the tensile experiments as well. Dislocation activity was rarely observed during either tensile or compressive experiments. Nevertheless, irreversible length and shape changes occurred during both the tension and compression of the Na dendrites. This is consistent with the notion of creep via atomic diffusion as the primary plastic deformation mechanism of soft Na metal at room temperature, as suggested by Fincher et al.[21]

Under prolonged ebeam irradiation in a CO_2 environment, the surface layer of the Na dendrite grew thicker due to the continued reaction of Na with CO_2. Eventually, the whole Na dendrite turned into a Na_2CO_3 pillar, as exemplified in Figure 7. As Na climbed up along the CNT, it was transformed almost entirely into Na_2CO_3 (Figure 7a−f, Movie S18), with only minor Na residue, as indicated by the EDP (Figure 7f). The Na_2CO_3 pillar is strongly tapered (Figure 7e), with the upper end much thinner than the lower end. The tapering implies that the growth of the Na_2CO_3 pillar was rate-limited by Na^+ ion transport because the lower end was closer to the Na source than the upper end and thus received Na earlier, resulting in faster local growth and a larger cross section. The tapering also suggests that Na_2CO_3 might not be a good ionic conductor because otherwise, the tapering would not develop. To measure its mechanical properties, the as-grown Na_2CO_3 pillar was subjected to *in situ* compression testing (Figure 7g−j, Movie S19). No obvious changes in the shape and contrast of the pillar were detected during *in situ* compression, but the pillar remained slightly bent after the release of the load (Figure 7j). The maximum compressive force was 4.02 μN (Figure 7k). When we used the midsection diameter to estimate the cross-sectional area, the compressive strength was calculated to be 261 MPa. Figure 7l−o (Movie S20) shows the compression experiment on another Na_2CO_3 nanopillar. The maximum compressive force was 0.42 μN (Figure 7p). Using the midsection diameter as the cross-sectional area, the compressive strength was calculated to be 336 MPa.

Figure 8 (Movie S21) shows the *in situ* compression experiment conducted on a hollow Na_2CO_3 nanosphere, which was formed by the ebeam irradiation of a Na nanosphere in a CO_2 atmosphere, and the outward diffusion of Na caused the formation of the hollow geometry. The reduction of CO_2 by the ebeam on the surface and the outward diffusion of Na^+ across the Na_2CO_3 layer continuously thicken the Na_2CO_3 layer and consume the Na in the core, finally forming the hollow Na_2CO_3. Both EDP (Figure 8e) and EELS (Figure 8f,g) confirm the hollowed nanoparticle to be Na_2CO_3. After compression, the hollow Na_2CO_3 nanosphere is slightly flattened (Figure 8d). The apparent yield strength is 692 MPa, as estimated from the nominal nanosphere size without considering the hollow interior. Overall, the maximum strength of all tested nanocrystalline Na dendrites ranges from 36 to 203 MPa, whereas that of Na_2CO_3 varies from 261 to 692 MPa (Table 1). Bulk metal Na is very soft; in fact, we easily

scratched Na with a W tip in the glovebox and used it as the anode in the present ETEM-AFM device. Fincher et al.[21] recently reported the yield strength of bulk Na to be between 0.1 and 0.25 MPa, and it can markedly increase with strain rate. The shear modulus of Na is reported to be 1.53 GPa.[32] In this work, the compressive/tensile strength measured from Na deposits stabilized by a Na_2CO_3 surface layer is much higher than that of bulk Na.[21] Fincher et al.[21] reported a strong size effect on the yield strength of bulk Na. In figure 8 of their paper, the yield strength of Na increases from ∼0.3 to ∼8 MPa when the length scale decreases from ∼10^4 to ∼45 μm. Previous experiments of Li dendrites also showed strong size effects, which became particularly prominent in the nanometer regime.[23,33,34] For example, our previous *in situ* ETAM-AFM experiment showed that the yield strength of Li dendrites can be >200 times that of bulk Li. Hence the drastically different mechanical properties between the bulk and nanoscale alkali metals underscore the importance of the direct investigation of their mechanical response under conditions similar to battery-operating environments, namely, under the combined electro-chemo-mechanical loading and with nanoscale dimensions. Our current results of Na dendrites are aligned with the recent results of Li dendrites by Zhang et al.,[35] which have shown that *in situ* plated Li dendrites have a higher yield strength (with and without the applied overpotential) and a lower creep rate compared with bulk Li. Therefore, the quantitative characterization of mechanical properties for both bulk and small-volume Li and Na is crucially important because the results will provide baseline data and insight toward understanding their electro-chemo-mechanical behavior under the operating conditions of SMBs/LMBs.[21,36−38]

Solid Na possesses a low activation energy of atomic diffusion (42 kJ/mol^{-1}, with a low melting temperature of 371 K).[32] Thus room temperature corresponds to a homologous temperature of 0.8. At such a high homologous temperature, pure metals often creep by either Coble creep or Nabarro−Herring creep. Both mechanisms involve atomic diffusion and could become highly active during the plastic flow of Na dendrites, given the lack of observed dislocation activity during *in situ* TEM compression experiments. Future studies are necessary to resolve the exact mechanism and the impact of creep deformation on the mechanical response of Na dendrites.

In all solid-state Li battery, a short circuit[39−46] is thought to be caused by mechanically strong Li dendrites piercing through solid electrolytes.[45,47−50] It has been suggested that solid electrolytes with high elastic moduli may suppress the dendrite growth, thus mitigating the dendrite-induced shorting of the battery. By considering the battery system of the Li anode and the polymer electrolyte and using the linear elastic theory, Monroe and Newman[51] predicted that if the shear modulus of the polymer electrolyte is two times bigger than that of Li, then the dendrite growth can be suppressed. This prediction has stimulated extensive studies of solid electrolytes with high mechanical stiffness to inhibit dendrite growth. However, hitherto suppressing the dendrite growth in a Li-metal-based solid-state battery has not been successful.[52] In fact, experiments show that the typical solid electrolytes such as $Li_7La_3Zr_2O_{12}$ (LLZO) and $Li_{10}GeP_2S_{12}$ (LGPS) fail to suppress the dendrite growth despite their large elastic moduli.[53] The discrepancy between the theoretical prediction by Newman and Monroe and the experimental results can be attributed to the following two factors. First, the former is

based on a linear elastic theory, but our work shows that plasticity plays an important role in the deformation of Na. Second, the former is based on a perfect electrolyte, whereas practical solid electrolytes have unavoidable flaws such as micropores and microcracks, which significantly affect the dendrite growth.[51,54−56]

The densification of practical solid electrolytes is usually not ideal, such that pores/voids, grain boundaries, and surface cracks commonly exist. These structural defects can critically affect the growth and flow of Li or Na dendrites as they infiltrate through solid electrolytes. The stress induced by Li or Na deposition in the confined volumes of structural defects can be very high. For example, the stress σ_{ecm} due to Li or Na deposition in a surface crack in a solid electrolyte under an overpotential $\Delta\phi$ can be calculated using the following equation[55]

$$\sigma_{ecm}V_m = F\Delta\phi \qquad (3)$$

where σ_{ecm} is the electro-chemo-mechanical stress, F is Faraday's constant ($F = 9.65 \times 10^4$ C mol^{-1}), and V_m is the molar volume of Li or Na metals ($V_m = 13$ cm^3 mol^{-1} for Li and 23.7 cm^3 mol^{-1} for Na).[55] Equation 3 relates the electrochemical work (right side of the equation) to the mechanical work (left side of the equation), and it forms the basis for predicting the overpotential-induced stress under mechanical confinement. For example, an overpotential of $\Delta\phi = 100$ mV can generate a mechanical stress of $\sigma = 750$ MPa in Li and 412 MPa in Na, which may cause crack propagation in a solid electrolyte.[57−60] The large stress generated by the overpotential-driven growth of Li and Na may cause Li and Na metals to creep by diffusion. At room temperature, the homologous temperature is $T/T_m = 0.65$ for Li and 0.8 for Na. Given such high homologous temperatures, Li and Na should exhibit a large creep strain rate, according to the deformation mechanism map of metals.[61] Creep of pure Li or Na[59] is driven by the large mechanical stress generated by overpotential according to eq 3. This suggests that under a high overpotential, Li and Na may "flow", transferring large stress generated by the overpotential to the surrounding medium such as solid electrolytes. Consequently, flaws such as micropores and microcracks are detrimental, as Li and Na can infiltrate into these free spaces.

The fracture stress σ_f of a ceramic solid electrolyte can be calculated using the following equation[23,62−64]

$$\sigma_f = K_{IC}(\pi a_c)^{-1/2} \qquad (4)$$

where K_{IC} denotes the fracture toughness of solid electrolyte and a_c is the critical flaw size such as the pore or grain size. Consider the solid electrolyte of LLZO as an example.[65] Suppose a typical pore size in LLZO is ~5 μm, and the fracture toughness K_{IC} of LLZO is ~1 MPa m$^{1/2}$.[62] Plugging these values into eq 4 yields $\sigma_f \approx 150$ MPa. According to eq 3, an overpotential of only 33 mV would produce such a critical stress to cause the fracture of LLZO. From eq 4, it is seen that as the flaw size decreases, the critical fracture stress increases, suggesting that reducing the flaw size such as the pore size can suppress crack propagation and thus dendrite penetration.

In the case of an SMB such as a sodium−sulfur (Na−S) battery,[66−70] Na-β-alumina is used as the solid electrolyte because it has a high ionic conductivity and is one of the most stable Na ion conductors.[19,71−74] The fracture toughness K_{IC} of Na-β-alumina is ~2 MPa m$^{1/2}$;[75] according to eq 4, the fracture stress σ_f is ~357 MPa for a 10 μm long crack, which

requires an overpotential of 86.7 mV to generate such a stress. Such an overpotential is attainable in an SMB. Furthermore, a crack or pore size of 10 μm can be easily identified in a solid electrolyte.[76] Hence Na dendrites can grow and flow by creep through these large cracks to cause a short circuit of the solid electrolyte.[55,65,77] In fact, Na dendrites that propagate through large cracks in Na-β-alumina were indeed observed by TEM.[77−79] From an electro-chemo-mechanical perspective, the remedy is to reduce flaw sizes in solid electrolytes and overpotentials. This requires advanced materials processing technology and also interface engineering between the electrode and the electrolyte. For example, if the flaw size is reduced to 500 nm, then σ_f increases to 798 MPa, and an overpotential >100 mV is required to generate such a high stress.

In summary, we report the real-time observations of Na dendrite growth with simultaneous mechanical measurements using a novel ETEM-AFM platform. We control the *in situ* growth of Na dendrites (stabilized by a Na$_2$CO$_3$ surface SEI layer) with a diameter of a few hundreds of nanometers and measure the elastic−plastic properties of individual Na dendrites with and without electrochemical driving forces. Inside the gas environment of ETEM, a nanometer-thick Na$_2$CO$_3$ forms on the surface of *in situ* grown Na dendrites. Such an ultrathin Na$_2$CO$_3$ layer stabilizes the reactive Na metal and prevents electron-beam damage, thereby enabling *in situ* imaging and mechanical testing. The measured maximum strength of Na dendrite reaches as high as 203 MPa, which is >300 times that of bulk Na. It shows that the electrochemical process of Na deposits (stabilized by a Na$_2$CO$_3$ surface layer) can generate high stress in Na, which would cause the creep of Na through defects such as cracks and pores in solid electrolytes, leading to the failure of solid-state Na batteries. Consequently, reducing the flaw size in solid electrolytes is critical to mitigating Na dendrite-induced failure in solid-state SMBs. Altogether, the results in this work provide important insight for mitigating a dendrite-induced short circuit in solid-state SMBs.

■ ASSOCIATED CONTENT

ⓢ Supporting Information

The Supporting Information is available free of charge at https://pubs.acs.org/doi/10.1021/acsenergylett.0c01214.

> Supplementary Methods. *In situ* ETEM-AFM, synthesis of arc-discharged CNTs, effects of surface Na$_2$CO$_3$ layer on the mechanical properties of Na dendrites, molar volume calculation of Li and Na, and quantification of bending off the image plane. Figure S1. Na substrate covered by a Na$_2$CO$_3$ SEI layer with a thickness of 110−140 nm and Na nanospheres grown on the Na substrate. Low-loss and a core-loss EELS of the Na substrate. Figure S2. Growth thickness of the Na$_2$CO$_3$ layer versus time for four typical Na dendrites. Figure S3. *In situ* TEM images of the Na dendrite growth. Current flowing in the dendrite. Figure S4. Time-lapse TEM images showing the growth of a Na nanorod via electrochemical plating. EDP of the Na dendrite. Dark-field image of the Na dendrite formed by selecting the (110) reflections in the EDP. Low-loss and core-loss EELS showing the characteristics of Na. Figure S5. Time-lapse TEM images showing the growth of a Na nanocube via electrochemical plating. EDP of the Na nanocube. The

nanocube appears to be heavily strained, suggesting there exists significant diffusion induced stress during the growth. Figure S6. Na dendrite was exposed to ebeam irradiation for 887 s in a CO_2 ambient, showing no discernible irradiation damage due to the protection of the surface Na_2CO_3 layer. Under no gas condition, the dendrite only grew with a Na plate. Figure S7. Sequential TEM images showing the compression process and the corresponding force-displacement of a Na nanorod. Figure S8. Two sets of *in situ* compression tests of as-grown Na dendrites. Figure S9. Three sets of *in situ* tensile tests of as-grown Na dendrites. Figure S10. Tilting the as-grown Na dendrite from −14.8 to 27.2°. Figure S11. Tilting the as-grown Na dendrite from −12.9 to 29.4°. Figure S12. Tilting the as-grown Na nanorod from 3.1 to −28.6°. Table S1. Mechanical data corresponding to Figure 4. Table S2. Mechanical data corresponding to Figure S7. Table S3. Mechanical data corresponding to Figure 5. References (PDF)

Movie S1. *In situ* TEM movie showing the growth of a Na dendrite (Figure 1) (AVI)

Movie S2. *In situ* TEM movie showing the growth of a Na dendrite (Figure 2a−e) (AVI)

Movie S3. *In situ* TEM movie showing the growth of a Na dendrite under different potentials (Figure 2m−s) (AVI)

Movie S4. *In situ* TEM movie showing the growth of a Na dendrite (Figure 3a−d) (AVI)

Movie S5. *In situ* TEM movie showing the growth of a Na dendrite (Figure 3e−h) (AVI)

Movie S6. *In situ* TEM movie showing the growth of the Na nanocube (Figure 3i−l) (AVI)

Movie S7. *In situ* TEM movie showing the growth of a Na nanorod (Figure S4a−d) (AVI)

Movie S8. *In situ* TEM movie showing the growth of a Na nanocube (Figure S5a−d) (AVI)

Movie S9. Assessing the mechanical properties of a Na dendrite by *in situ* compression (Figure 4c) (AVI)

Movie S10. Measuring the mechanical properties of a Na nanoparticle by *in situ* compression (Figure 5a) (AVI)

Movie S11. Assessing the mechanical properties of a Na dendrite by *in situ* tensile test (Figure 6a−d) (AVI)

Movie S12. Assessing the mechanical properties of a Na nanorod by *in situ* compression (Figure S7a) (AVI)

Movie S13. Assessing the mechanical properties of a Na nanosphere by *in situ* compression (Figure S8a−c) (AVI)

Movie S14. Assessing the mechanical properties of a Na nanosphere by *in situ* compression (Figure S8d−f) (AVI)

Movie S15. Assessing the mechanical properties of a Na nanosphere by *in situ* tensile deformation (Figure S9a−d) (AVI)

Movie S16. Assessing the mechanical properties of a Na nanosphere by *in situ* tensile deformation (Figure S9e−h) (AVI)

Movie S17. Assessing the mechanical properties of a Na nanorod by *in situ* tensile deformation (Figure S9i−k) (AVI)

Movie S18. *In situ* TEM movie showing the growth of a Na_2CO_3 pillar (Figure 7a−e) (AVI)

Movie S19. Assessing the mechanical properties of a Na_2CO_3 pillar (Figure 7g−j) (AVI)

Movie S20. Assessing the mechanical properties of another Na_2CO_3 pillar (Figure 7k−n) (AVI)

Movie S21. Assessing the mechanical properties of a Na_2CO_3 nanosphere by *in situ* compression (Figure 8a−d) (AVI)

■ AUTHOR INFORMATION

Corresponding Authors

Liqiang Zhang − *Clean Nano Energy Center, State Key Laboratory of Metastable Materials Science and Technology, Yanshan University, Qinhuangdao 066004, P. R. China;* Email: liqiangzhang85@163.com

Yongfu Tang − *Clean Nano Energy Center, State Key Laboratory of Metastable Materials Science and Technology and Hebei Key Laboratory of Applied Chemistry, College of Environmental and Chemical Engineering, Yanshan University, Qinhuangdao 066004, P. R. China;* orcid.org/0000-0002-6318-3110; Email: tangyongfu@ysu.edu.cn

Jianyu Huang − *Clean Nano Energy Center, State Key Laboratory of Metastable Materials Science and Technology, Yanshan University, Qinhuangdao 066004, P. R. China; School of Materials Science and Engineering, Xiangtan University, Xiangtan, Hunan 411105, P. R. China;* orcid.org/0000-0002-8424-5368; Email: jyhuang8@hotmail.com

Authors

Qiunan Liu − *Clean Nano Energy Center, State Key Laboratory of Metastable Materials Science and Technology, Yanshan University, Qinhuangdao 066004, P. R. China*

Haiming Sun − *Clean Nano Energy Center, State Key Laboratory of Metastable Materials Science and Technology, Yanshan University, Qinhuangdao 066004, P. R. China;* orcid.org/0000-0001-9085-500X

Lin Geng − *Clean Nano Energy Center, State Key Laboratory of Metastable Materials Science and Technology, Yanshan University, Qinhuangdao 066004, P. R. China*

Yanshuai Li − *Clean Nano Energy Center, State Key Laboratory of Metastable Materials Science and Technology, Yanshan University, Qinhuangdao 066004, P. R. China*

Yushu Tang − *Institute of Nanotechnology (INT), Karlsruhe Institute of Technology (KIT), 76344 Eggenstein-Leopoldshafen, Germany*

Peng Jia − *Clean Nano Energy Center, State Key Laboratory of Metastable Materials Science and Technology, Yanshan University, Qinhuangdao 066004, P. R. China*

Zaifa Wang − *Clean Nano Energy Center, State Key Laboratory of Metastable Materials Science and Technology, Yanshan University, Qinhuangdao 066004, P. R. China*

Qiushi Dai − *Clean Nano Energy Center, State Key Laboratory of Metastable Materials Science and Technology, Yanshan University, Qinhuangdao 066004, P. R. China*

Tongde Shen − *Clean Nano Energy Center, State Key Laboratory of Metastable Materials Science and Technology, Yanshan University, Qinhuangdao 066004, P. R. China*

Ting Zhu − *Woodruff School of Mechanical Engineering, Georgia Institute of Technology, Atlanta, Georgia 30332, United States*

Complete contact information is available at:
https://pubs.acs.org/10.1021/acsenergylett.0c01214

Notes

The authors declare no competing financial interest.

■ REFERENCES

(1) Yang, Z.; Zhang, J.; Kintner-Meyer, M. C. W.; Lu, X.; Choi, D.; Lemmon, J. P.; Liu, J. Electrochemical Energy Storage for Green Grid. *Chem. Rev.* **2011**, *111* (5), 3577−3613.

(2) Pan, H.; Hu, Y.-S.; Chen, L. Room-Temperature Stationary Sodium-Ion Batteries for Large-Scale Electric Energy Storage. *Energy Environ. Sci.* **2013**, *6* (8), 2338−2360.

(3) Palomares, V.; Casas-Cabanas, M.; Castillo-Martínez, E.; Han, M. H.; Rojo, T. Update on Na-Based Battery Materials. A Growing Research Path. *Energy Environ. Sci.* **2013**, *6* (8), 2312−2337.

(4) Matsuo, M.; Nakamori, Y.; Orimo, S.-i.; Maekawa, H.; Takamura, H. Lithium Superionic Conduction in Lithium Borohydride Accompanied by Structural Transition. *Appl. Phys. Lett.* **2007**, *91* (22), 224103.

(5) Chi, S.-S.; Qi, X.-G.; Hu, Y.-S.; Fan, L.-Z. 3d Flexible Carbon Felt Host for Highly Stable Sodium Metal Anodes. *Adv. Energy Mater.* **2018**, *8* (15), 1702764.

(6) Han, M. H.; Gonzalo, E.; Singh, G.; Rojo, T. A Comprehensive Review of Sodium Layered Oxides: Powerful Cathodes for Na-Ion Batteries. *Energy Environ. Sci.* **2015**, *8* (1), 81−102.

(7) Xiang, X.; Zhang, K.; Chen, J. Recent Advances and Prospects of Cathode Materials for Sodium-Ion Batteries. *Adv. Mater.* **2015**, *27* (36), 5343−5364.

(8) Luo, W.; Shen, F.; Bommier, C.; Zhu, H.; Ji, X.; Hu, L. Na-Ion Battery Anodes: Materials and Electrochemistry. *Acc. Chem. Res.* **2016**, *49* (2), 231−240.

(9) Kundu, D.; Talaie, E.; Duffort, V.; Nazar, L. F. The Emerging Chemistry of Sodium Ion Batteries for Electrochemical Energy Storage. *Angew. Chem., Int. Ed.* **2015**, *54* (11), 3431−3448.

(10) Ponrouch, A.; Monti, D.; Boschin, A.; Steen, B.; Johansson, P.; Palacín, M. R. Non-Aqueous Electrolytes for Sodium-Ion Batteries. *J. Mater. Chem. A* **2015**, *3* (1), 22−42.

(11) Fang, Y.; Li, Z.; Huang, Y.; Zhang, S.; Nordlander, P.; Halas, N. J.; Xu, H. Branched Silver Nanowires as Controllable Plasmon Routers. *Nano Lett.* **2010**, *10* (5), 1950−1954.

(12) Hwang, J.-Y.; Myung, S.-T.; Sun, Y.-K. Sodium-Ion Batteries: Present and Future. *Chem. Soc. Rev.* **2017**, *46* (12), 3529−3614.

(13) Li, W.-J.; Chou, S.-L.; Wang, J.-Z.; Liu, H.-K.; Dou, S.-X. Simply Mixed Commercial Red Phosphorus and Carbon Nanotube Composite with Exceptionally Reversible Sodium-Ion Storage. *Nano Lett.* **2013**, *13* (11), 5480−5484.

(14) Yang, T.; Jia, P.; Liu, Q.; Zhang, L.; Du, C.; Chen, J.; Ye, H.; Li, X.; Li, Y.; Shen, T.; Tang, Y.; Huang, J. Air-Stable Lithium Spheres Produced by Electrochemical Plating. *Angew. Chem.* **2018**, *130* (39), 12932−12935.

(15) Yui, Y.; Hayashi, M.; Nakamura, J. In Situ Microscopic Observation of Sodium Deposition/Dissolution on Sodium Electrode. *Sci. Rep.* **2016**, *6* (1), 22406.

(16) Rodriguez, R.; Loeffler, K. E.; Nathan, S. S.; Sheavly, J. K.; Dolocan, A.; Heller, A.; Mullins, C. B. In Situ Optical Imaging of Sodium Electrodeposition: Effects of Fluoroethylene Carbonate. *ACS Energy Lett.* **2017**, *2* (9), 2051−2057.

(17) Wei, S.; Choudhury, S.; Xu, J.; Nath, P.; Tu, Z.; Archer, L. A. Highly Stable Sodium Batteries Enabled by Functional Ionic Polymer Membranes. *Adv. Mater.* **2017**, *29* (12), 1605512.

(18) Medenbach, L.; Bender, C. L.; Haas, R.; Mogwitz, B.; Pompe, C.; Adelhelm, P.; Schröder, D.; Janek, J. Origins of Dendrite Formation in Sodium-Oxygen Batteries and Possible Counter-Measures. *Energy Technol.* **2017**, *5* (12), 2265−2274.

(19) Spencer Jolly, D.; Ning, Z.; Darnbrough, J. E.; Kasemchainan, J.; Hartley, G. O.; Adamson, P.; Armstrong, D. E. J.; Marrow, J.; Bruce, P. G. Sodium/Na β″ Alumina Interface: Effect of Pressure on Voids. *ACS Appl. Mater. Interfaces* **2020**, *12* (1), 678−685.

(20) Bay, M.-C.; Wang, M.; Grissa, R.; Heinz, M. V. F.; Sakamoto, J.; Battaglia, C. Sodium Plating from Na-β″-Alumina Ceramics at Room Temperature, Paving the Way for Fast-Charging All-Solid-State Batteries. *Adv. Energy Mater.* **2020**, *10* (3), 1902899.

(21) Fincher, C. D.; Zhang, Y.; Pharr, G. M.; Pharr, M. Elastic and Plastic Characteristics of Sodium Metal. *ACS Appl. Energy Mater.* **2020**, *3* (2), 1759−1767.

(22) He, Y.; Ren, X.; Xu, Y.; Engelhard, M. H.; Li, X.; Xiao, J.; Liu, J.; Zhang, J.-G.; Xu, W.; Wang, C. Origin of Lithium Whisker Formation and Growth under Stress. *Nat. Nanotechnol.* **2019**, *14* (11), 1042−1047.

(23) Zhang, L.; Yang, T.; Du, C.; Liu, Q.; Tang, Y.; Zhao, J.; Wang, B.; Chen, T.; Sun, Y.; Jia, P.; Li, H.; Geng, L.; Chen, J.; Ye, H.; Wang, Z.; Li, Y.; Sun, H.; Li, X.; Dai, Q.; Tang, Y.; Peng, Q.; Shen, T.; Zhang, S.; Zhu, T.; Huang, J. Lithium Whisker Growth and Stress Generation in an in Situ Atomic Force Microscope−Environmental Transmission Electron Microscope Set-Up. *Nat. Nanotechnol.* **2020**, *15* (2), 94−98.

(24) Zhang, L.; Tang, Y.; Liu, Q.; Yang, T.; Du, C.; Jia, P.; Wang, Z.; Tang, Y.; Li, Y.; Shen, T.; Huang, J. Probing the Charging and Discharging Behavior of K-CO₂ Nanobatteries in an Aberration Corrected Environmental Transmission Electron Microscope. *Nano Energy* **2018**, *53*, 544−549.

(25) Darwiche, A.; Bodenes, L.; Madec, L.; Monconduit, L.; Martinez, H. Impact of the Salts and Solvents on the SEI Formation in Sb/Na Batteries: An XPS Analysis. *Electrochim. Acta* **2016**, *207*, 284−292.

(26) Bagley, E. Hooke's Law in Shear and Polymer Melt Fracture. *J. Appl. Phys.* **1960**, *31* (6), 1126−1127.

(27) Lu, Y.; Huang, J. Y.; Wang, C.; Sun, S.; Lou, J. Cold Welding of Ultrathin Gold Nanowires. *Nat. Nanotechnol.* **2010**, *5* (3), 218−224.

(28) Zhang, L.; Tang, Y.; Peng, Q.; Yang, T.; Liu, Q.; Wang, Y.; Li, Y.; Du, C.; Sun, Y.; Cui, L.; Yang, F.; Shen, T.; Shan, Z.; Huang, J. Ceramic Nanowelding. *Nat. Commun.* **2018**, *9* (1), 96.

(29) Hertz, H. Translated and Reprinted in English in "Hertz's Miscellaneous Papers" (Macmillan, New York, 1896) Ch. 5. *J. Reine Angew. Math.* **1881**, *92*, 156.

(30) Xiang, B.; Wang, L.; Liu, G.; Minor, A. M. Electromechanical Probing of Li/Li₂CO₃ core/Shell Particles in a TEM. *J. Electrochem. Soc.* **2013**, *160* (3), A415−A419.

(31) Mook, W. M.; Nowak, J. D.; Perrey, C. R.; Carter, C. B.; Mukherjee, R.; Girshick, S. L.; McMurry, P. H.; Gerberich, W. W. Compressive Stress Effects on Nanoparticle Modulus and Fracture. *Phys. Rev. B: Condens. Matter Mater. Phys.* **2007**, *75* (21), 214112.

(32) Sargent, P. M.; Ashby, M. F. Deformation Mechanism Maps for Alkali Metals. *Scr. Metall.* **1984**, *18* (2), 145−150.

(33) Fincher, C. D.; Ojeda, D.; Zhang, Y.; Pharr, G. M.; Pharr, M. Mechanical Properties of Metallic Lithium: From Nano to Bulk Scales. *Acta Mater.* **2020**, *186*, 215−222.

(34) Herbert, E. G.; Hackney, S. A.; Thole, V.; Dudney, N. J.; Phani, P. S. Nanoindentation of High-Purity Vapor Deposited Lithium Films: A Mechanistic Rationalization of Diffusion-Mediated Flow. *J. Mater. Res.* **2018**, *33* (10), 1347−1360.

(35) Zhang, X.; Wang, Q. J.; Harrison, K. L.; Jungjohann, K.; Boyce, B. L.; Roberts, S. A.; Attia, P. M.; Harris, S. J. Rethinking How

External Pressure Can Suppress Dendrites in Lithium Metal Batteries. *J. Electrochem. Soc.* **2019**, *166* (15), A3639−A3652.

(36) LePage, W. S.; Chen, Y.; Kazyak, E.; Chen, K.-H.; Sanchez, A. J.; Poli, A.; Arruda, E. M.; Thouless, M. D.; Dasgupta, N. P. Lithium Mechanics: Roles of Strain Rate and Temperature and Implications for Lithium Metal Batteries. *J. Electrochem. Soc.* **2019**, *166* (2), A89−A97.

(37) Herbert, E. G.; Dudney, N. J.; Rochow, M.; Thole, V.; Hackney, S. A. On the Mechanisms of Stress Relaxation and Intensification at the Lithium/Solid-State Electrolyte Interface. *J. Mater. Res.* **2019**, *34* (21), 3593−3616.

(38) Masias, A.; Felten, N.; Garcia-Mendez, R.; Wolfenstine, J.; Sakamoto, J. Elastic, Plastic, and Creep Mechanical Properties of Lithium Metal. *J. Mater. Sci.* **2019**, *54* (3), 2585−2600.

(39) Han, F.; Westover, A. S.; Yue, J.; Fan, X.; Wang, F.; Chi, M.; Leonard, D. N.; Dudney, N. J.; Wang, H.; Wang, C. High Electronic Conductivity as the Origin of Lithium Dendrite Formation within Solid Electrolytes. *Nature Energy* **2019**, *4* (3), 187−196.

(40) Sharafi, A.; Meyer, H. M.; Nanda, J.; Wolfenstine, J.; Sakamoto, J. Characterizing the Li−Li$_7$La$_3$Zr$_2$O$_{12}$ Interface Stability and Kinetics as a Function of Temperature and Current Density. *J. Power Sources* **2016**, *302*, 135−139.

(41) Cheng, L.; Chen, W.; Kunz, M.; Persson, K.; Tamura, N.; Chen, G.; Doeff, M. Effect of Surface Microstructure on Electrochemical Performance of Garnet Solid Electrolytes. *ACS Appl. Mater. Interfaces* **2015**, *7* (3), 2073−2081.

(42) Tsai, C.-L.; Roddatis, V.; Chandran, C. V.; Ma, Q.; Uhlenbruck, S.; Bram, M.; Heitjans, P.; Guillon, O. Li$_7$La$_3$Zr$_2$O$_{12}$ Interface Modification for Li Dendrite Prevention. *ACS Appl. Mater. Interfaces* **2016**, *8* (16), 10617−10626.

(43) Yonemoto, F.; Nishimura, A.; Motoyama, M.; Tsuchimine, N.; Kobayashi, S.; Iriyama, Y. Temperature Effects on Cycling Stability of Li Plating/Stripping on Ta-Doped Li$_7$La$_3$Zr$_2$O$_{12}$. *J. Power Sources* **2017**, *343*, 207−215.

(44) Garcia-Mendez, R.; Mizuno, F.; Zhang, R.; Arthur, T. S.; Sakamoto, J. Effect of Processing Conditions of 75Li$_2$S-25P$_2$S$_5$ Solid Electrolyte on Its Dc Electrochemical Behavior. *Electrochim. Acta* **2017**, *237*, 144−151.

(45) Han, F.; Yue, J.; Zhu, X.; Wang, C. Suppressing Li Dendrite Formation in Li$_2$S-P$_2$S$_5$ Solid Electrolyte by Li Incorporation. *Adv. Energy Mater.* **2018**, *8* (18), 1703644.

(46) Taylor, N. J.; Stangeland-Molo, S.; Haslam, C. G.; Sharafi, A.; Thompson, T.; Wang, M.; Garcia-Mendez, R.; Sakamoto, J. Demonstration of High Current Densities and Extended Cycling in the Garnet Li$_7$La$_3$Zr$_2$O$_{12}$ Solid Electrolyte. *J. Power Sources* **2018**, *396*, 314−318.

(47) Liu, H.; Cheng, X.-B.; Huang, J.-Q.; Yuan, H.; Lu, Y.; Yan, C.; Zhu, G.-L.; Xu, R.; Zhao, C.-Z.; Hou, L.-P.; He, C.; Kaskel, S.; Zhang, Q. Controlling Dendrite Growth in Solid-State Electrolytes. *ACS Energy Lett.* **2020**, *5* (3), 833−843.

(48) Fu, J.; Yu, P.; Zhang, N.; Ren, G.; Zheng, S.; Huang, W.; Long, X.; Li, H.; Liu, X. In Situ Formation of a Bifunctional Interlayer Enabled by a Conversion Reaction to Initiatively Prevent Lithium Dendrites in a Garnet Solid Electrolyte. *Energy Environ. Sci.* **2019**, *12* (4), 1404−1412.

(49) Zhang, Z.; Zhang, L.; Liu, Y.; Wang, H.; Yu, C.; Zeng, H.; Wang, L.-m.; Xu, B. Interface-Engineered Li$_7$La$_3$Zr$_2$O$_{12}$-Based Garnet Solid Electrolytes with Suppressed Li-Dendrite Formation and Enhanced Electrochemical Performance. *ChemSusChem* **2018**, *11* (21), 3774−3782.

(50) Suzuki, Y.; Kami, K.; Watanabe, K.; Watanabe, A.; Saito, N.; Ohnishi, T.; Takada, K.; Sudo, R.; Imanishi, N. Transparent Cubic Garnet-Type Solid Electrolyte of Al$_2$O$_3$-Doped Li$_7$La$_3$Zr$_2$O$_{12}$. *Solid State Ionics* **2015**, *278*, 172−176.

(51) Monroe, C.; Newman, J. The Impact of Elastic Deformation on Deposition Kinetics at Lithium/Polymer Interfaces. *J. Electrochem. Soc.* **2005**, *152* (2), A396−A404.

(52) Xu, W.; Wang, J.; Ding, F.; Chen, X.; Nasybulin, E.; Zhang, Y.; Zhang, J.-G. Lithium Metal Anodes for Rechargeable Batteries. *Energy Environ. Sci.* **2014**, *7* (2), 513−537.

(53) Wang, L.; Menakath, A.; Han, F.; Wang, Y.; Zavalij, P. Y.; Gaskell, K. J.; Borodin, O.; Iuga, D.; Brown, S. P.; Wang, C.; Xu, K.; Eichhorn, B. W. Identifying the Components of the Solid−Electrolyte Interphase in Li-Ion Batteries. *Nat. Chem.* **2019**, *11* (9), 789−796.

(54) Kerman, K.; Luntz, A.; Viswanathan, V.; Chiang, Y.-M.; Chen, Z. Review—Practical Challenges Hindering the Development of Solid State Li Ion Batteries. *J. Electrochem. Soc.* **2017**, *164* (7), A1731−A1744.

(55) Porz, L.; Swamy, T.; Sheldon, B. W.; Rettenwander, D.; Frömling, T.; Thaman, H. L.; Berendts, S.; Uecker, R.; Carter, W. C.; Chiang, Y.-M. Mechanism of Lithium Metal Penetration through Inorganic Solid Electrolytes. *Adv. Energy Mater.* **2017**, *7* (20), 1701003.

(56) Janek, J.; Zeier, W. G. A Solid Future for Battery Development. *Nature Energy* **2016**, *1* (9), 16141.

(57) Hull, D.; Rosenberg, H. M. The Deformation of Lithium, Sodium and Potassium at Low Temperatures: Tensile and Resistivity Experiments. *Philos. Mag.* **1959**, *4* (39), 303−315.

(58) Narayan, S.; Anand, L. A Large Deformation Elastic−Viscoplastic Model for Lithium. *Extreme Mech. Lett.* **2018**, *24*, 21−29.

(59) Chen, Y.; Wang, Z.; Li, X.; Yao, X.; Wang, C.; Li, Y.; Xue, W.; Yu, D.; Kim, S. Y.; Yang, F.; Kushima, A.; Zhang, G.; Huang, H.; Wu, N.; Mai, Y.-W.; Goodenough, J. B.; Li, J. Li Metal Deposition and Stripping in a Solid-State Battery Via Coble Creep. *Nature* **2020**, *578* (7794), 251−255.

(60) Armstrong, R. D.; Dickinson, T.; Turner, J. The Breakdown of β-Alumina Ceramic Electrolyte. *Electrochim. Acta* **1974**, *19* (5), 187−192.

(61) Ashby, M. F.; Jones, D. R. H. *Engineering Materials 1: An Introduction to Properties, Applications and Design*; Butterworth-Heinemann: Boston, 2012; Vol. *1*.

(62) Wolfenstine, J.; Allen, J. L.; Sakamoto, J.; Siegel, D. J.; Choe, H. Mechanical Behavior of Li-Ion-Conducting Crystalline Oxide-Based Solid Electrolytes: A Brief Review. *Ionics* **2018**, *24* (5), 1271−1276.

(63) Chiang, Y.-M.; Birnie, D. P.; Kingery, W. D. *Physical Ceramics*; J. Wiley: New York, 1997; Vol. *14*.

(64) Barsoum, M. W. *Fundamentals of Ceramics*; The McGraw Hill Companies, Inc.: New York, 1997.

(65) Ren, Y.; Shen, Y.; Lin, Y.; Nan, C.-W. Direct Observation of Lithium Dendrites inside Garnet-Type Lithium-Ion Solid Electrolyte. *Electrochem. Commun.* **2015**, *57*, 27−30.

(66) Xin, S.; Yin, Y.-X.; Guo, Y.-G.; Wan, L.-J. A High-Energy Room-Temperature Sodium-Sulfur Battery. *Adv. Mater.* **2014**, *26* (8), 1261−1265.

(67) Xu, X.; Zhou, D.; Qin, X.; Lin, K.; Kang, F.; Li, B.; Shanmukaraj, D.; Rojo, T.; Armand, M.; Wang, G. A Room-Temperature Sodium−Sulfur Battery with High Capacity and Stable Cycling Performance. *Nat. Commun.* **2018**, *9* (1), 3870.

(68) Yu, X.; Manthiram, A. Capacity Enhancement and Discharge Mechanisms of Room-Temperature Sodium−Sulfur Batteries. *ChemElectroChem* **2014**, *1* (8), 1275−1280.

(69) Ma, D.; Li, Y.; Yang, J.; Mi, H.; Luo, S.; Deng, L.; Yan, C.; Rauf, M.; Zhang, P.; Sun, X.; Ren, X.; Li, J.; Zhang, H. New Strategy for Polysulfide Protection Based on Atomic Layer Deposition of TiO$_2$ onto Ferroelectric-Encapsulated Cathode: Toward Ultrastable Free-Standing Room Temperature Sodium−Sulfur Batteries. *Adv. Funct. Mater.* **2018**, *28* (11), 1705537.

(70) Wenzel, S.; Metelmann, H.; Raiß, C.; Dürr, A. K.; Janek, J.; Adelhelm, P. Thermodynamics and Cell Chemistry of Room Temperature Sodium/Sulfur Cells with Liquid and Liquid/Solid Electrolyte. *J. Power Sources* **2013**, *243*, 758−765.

(71) Wenzel, S.; Leichtweiss, T.; Weber, D. A.; Sann, J.; Zeier, W. G.; Janek, J. Interfacial Reactivity Benchmarking of the Sodium Ion Conductors Na$_3$PS$_4$ and Sodium B-Alumina for Protected Sodium Metal Anodes and Sodium All-Solid-State Batteries. *ACS Appl. Mater. Interfaces* **2016**, *8* (41), 28216−28224.

(72) Wu, T.; Wen, Z.; Sun, C.; Wu, X.; Zhang, S.; Yang, J. Disordered Carbon Tubes Based on Cotton Cloth for Modulating Interface Impedance in β''-Al$_2$O$_3$-Based Solid-State Sodium Metal Batteries. *J. Mater. Chem. A* **2018**, *6* (26), 12623−12629.

(73) Lacivita, V.; Wang, Y.; Bo, S.-H.; Ceder, G. Ab Initio Investigation of the Stability of Electrolyte/Electrode Interfaces in All-Solid-State Na Batteries. *J. Mater. Chem. A* **2019**, *7* (14), 8144−8155.

(74) Kummer, J. B-Alumina Electrolytes. *Prog. Solid State Chem.* **1972**, *7*, 141−175.

(75) Feldman, L. A.; De Jonghe, L. C. Initiation of Mode I Degradation in Sodium-Beta Alumina Electrolytes. *J. Mater. Sci.* **1982**, *17* (2), 517−524.

(76) Kato, A.; Nose, M.; Yamamoto, M.; Sakuda, A.; Hayashi, A.; Tatsumisago, M. Mechanical Properties of Sulfide Glasses in All-Solid-State Batteries. *J. Ceram. Soc. Jpn.* **2018**, *126* (9), 719−727.

(77) De Jonghe, L. C.; Feldman, L.; Millett, P. Some Geometrical Aspects of Breakdown of Sodium Beta Alumina. *Mater. Res. Bull.* **1979**, *14* (5), 589−595.

(78) De Jonghe, L. C.; Feldman, L.; Buechele, A. Failure Modes of Na-Beta Alumina. *Solid State Ionics* **1981**, *5*, 267−269.

(79) De Jonghe, L. C.; Feldman, L.; Beuchele, A. Slow Degradation and Electron Conduction in Sodium/Beta-Aluminas. *J. Mater. Sci.* **1981**, *16* (3), 780−786.